Enhanced ion transmission efficiency up to m/z 24 000 for MALDI Protein Imaging Mass Spectrometry

Prentice, Boone M.; Ryan, Daniel J.; Van De Plas, Raf; Caprioli, Richard M.; Spraggins, Jeffrey M.

DOI
10.1021/acs.analchem.7b05105

Publication date
2018

Document Version
Final published version

Published in
Analytical Chemistry

analytical chemistry

Article

Cite This: *Anal. Chem.* 2018, 90, 5090−5099

pubs.acs.org/ac

Enhanced Ion Transmission Efficiency up to *m/z* 24 000 for MALDI Protein Imaging Mass Spectrometry

Boone M. Prentice,[†,‡] Daniel J. Ryan,[§] Raf Van de Plas,[‡,⊥] Richard M. Caprioli,[†,‡,§,∥] and Jeffrey M. Spraggins*[,†,‡,§]

[†]Department of Biochemistry, [‡]Mass Spectrometry Research Center, [§]Department of Chemistry, and [∥]Department of Pharmacology and Medicine, Vanderbilt University and Vanderbilt University Medical Center, Nashville, Tennessee 37232, United States

[⊥]Delft Center for Systems and Control, Delft University of Technology, Delft 2628 CD, The Netherlands

Supporting Information

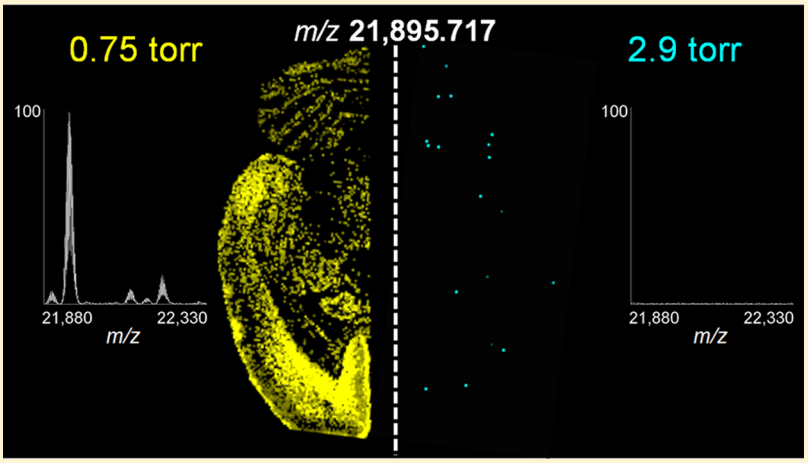

ABSTRACT: The molecular identification of species of interest is an important part of an imaging mass spectrometry (IMS) experiment. The high resolution accurate mass capabilities of Fourier transform ion cyclotron resonance mass spectrometry (FT-ICR MS) have recently been shown to facilitate the identification of proteins in matrix-assisted laser desorption/ionization (MALDI) IMS. However, these experiments are typically limited to proteins giving rise to ions of relatively low *m/z* due to difficulties transmitting and measuring large molecular weight ions of low charge states. Herein we have modified the source gas manifold of a commercial MALDI FT-ICR MS to regulate the gas flow and pressure to maximize the transmission of large *m/z* protein ions through the ion funnel region of the instrument. By minimizing the contribution of off-axis gas disruption to ion focusing and maximizing the effective potential wall confining the ions through pressure optimization, the signal-to-noise ratios (S/N) of most protein species were improved by roughly 1 order of magnitude compared to normal source conditions. These modifications enabled the detection of protein standards up to *m/z* 24 000 and the detection of proteins from tissue up to *m/z* 22 000 with good S/N, roughly doubling the mass range for which high quality protein ion images from rat brain and kidney tissue could be produced. Due to the long time-domain transients (>4 s) required to isotopically resolve high *m/z* proteins, we have used these data as part of an FT-ICR IMS-microscopy data-driven image fusion workflow to produce estimated protein images with both high mass and high spatial resolutions.

The ability to efficiently sample ions generated from relatively high pressure ion sources into the instrument vacuum chamber for analysis is a key factor in determining the overall sensitivity of a mass spectrometry experiment. The advent of ambient ionization methods such as electrospray ionization (ESI) has necessitated the development of improved methods of ion transmission across differentially pumped regions of the mass spectrometer.[1−8] The introduction of the ion funnel, which consists of a stack of closely spaced ring electrodes with successively decreasing inner diameters, has enabled ion transmission efficiencies that approach 100%.[9−11] Ion funnel interfaces are now present on many commercial mass spectrometers and can transmit ions with little *m/z* bias.[12−14] While extensive studies have been performed to characterize the fundamental mechanisms of ion transmission and focusing in ion funnels for ESI-generated ions,[15−19] relatively little work has been done to characterize the transmission efficiency of species generated by matrix-assisted laser desorption/ionization (MALDI), which can introduce unique considerations for ions of high *m/z* ratios.

Received: December 7, 2017
Accepted: February 14, 2018
Published: February 14, 2018

DOI: 10.1021/acs.analchem.7b05105
Anal. Chem. 2018, 90, 5090−5099

The efficiency of transport through the ion funnel is governed by several processes, including the collection of ions emanating from the source and the collisional focusing of these species in the ion funnel. Important to both of these processes are the gas flow dynamics and the operating pressure of the system.[10,16] Off-axis gas flow can detrimentally effect the collection of ions into the mass spectrometer, and the operating pressure of the ion funnel (along with its physical dimensions and operating RF voltages) determines the effective electric field for ion confinement.[15,16] At increased operating pressures, the effective potential well for ions is suppressed and a decrease in ion radial confinement is observed.[20] This situation is especially pronounced for ions of high m/z values (greater than 10 000) that have shallower pseudopotential well depths.[19,21,22] Most ESI-based experiments analyze ions in a more modest mass range from m/z 200 to 3000, such as analyses of singly charged metabolites and lipids and multiply charged peptides and proteins. Especially for high m/z species generated by ESI (e.g., intact protein complexes), additional processes such as ion desolvation become important to consider when determining the operating parameters of the source.[15,23−25] Even these high molecular weight complexes are typically multiply charged and thus of relatively modest m/z value, perhaps explaining the scarcity of reports detailing the use of ion funnels to study ions in excess of $m/z \sim 10\,000$.[26−28] In contrast to ESI, MALDI-generated proteins are typically observed at low charge states (i.e., higher m/z) and do not undergo desolvation, although declustering during MALDI plume evolution could be an analogous process in this context.[29−31]

Recently, we have reported the detection of protein ions in an imaging mass spectrometry (IMS) experiment up to $m/z \sim$ 12 000 with good signal-to-noise ratios (S/N), and up to m/z 17 000 with low S/N, using a commercial ion funnel-based MALDI source on a Fourier transform ion cyclotron resonance (FT-ICR) mass spectrometer.[32] While FT-ICR instruments have been widely used to study a variety of low molecular weight MALDI-generated ions,[33−37] intact protein analysis by MALDI has historically been performed on time-of-flight (TOF) mass spectrometers due to the superior sensitivity of these platforms at high m/z ratios.[38,39] Most MALDI TOF instruments generally operate at high vacuum, making them incompatible with current ion funnel designs that typically operate at pressures of 0.1−30 Torr (~0.1−40 mbar). Despite the superior sensitivity of TOF-based platforms, the high mass resolving power and mass accuracy afforded by FT-ICR instruments have recently been demonstrated to facilitate the identification of isotopically resolved, MALDI-generated intact proteins in a complex mixture of species detected during a tissue imaging experiment.[32,40,41] Early work by several groups noted the benefits of FT-ICR to studying high m/z ions generated using internal MALDI sources (i.e., located in the ultrahigh vacuum region of the ICR cell).[42−44] Although relatively little research has focused on high m/z species generated by external MALDI sources due to inefficient ion transmission, advances in ion optics and the use of stronger magnetic fields are now enabling these types of experiments.

Herein we have modified the source region of a 15T FT-ICR mass spectrometer to maximize the ion funnel transmission efficiency of high m/z MALDI-generated protein ions. The dual ESI/MALDI ion source on this instrument was modified to allow for control of the existing gas flow and pressure, both of which were identified to be important to ion transmission. Significant improvements in ion transmission efficiency were observed for protein standards up to $m/z \sim 24\,000$ and for proteins detected from tissue up to m/z 22 000, roughly doubling the normal mass range and dramatically enhancing the quality of the protein imaging data.

EXPERIMENTAL SECTION

Materials. 2,5-Dihydroxyacetphenone (DHA) MALDI matrix, insulin, ubiquitin, cytochrome C, apomyoglobin, trypsinogen, hematoxylin stain, glycerol, and aluminum potassium sulfate were purchased from Sigma-Aldrich (St. Louis, MO). Ethanol, methanol, chloroform, acetonitrile (ACN), formic acid (FA), and acetic acid were purchased from Fisher Scientific (Pittsburgh, PA). A standard mixture of insulin (0.25 pmol/μL), ubiquitin (1 pmol/μL), cytochrome C (1 pmol/μL), apomyoglobin (2 pmol/μL), and trypsinogen (4 pmol/μL) was prepared and mixed 1:1 with a 15 mg/mL DHA solution (90/10/0.1, ACN/H_2O/FA). One microliter aliquots of this mixture were manually spotted onto a MTP AnchorChip MALDI target (Bruker Daltonics) and allowed to dry. Rat brain and rat kidney were both purchased from Pel-Freeze Biologicals (Rogers, AR) and stored at −80 °C until analysis.

Mass Spectrometry. All experiments were performed on a 15T solariX XR FT-ICR mass spectrometer equipped with an Apollo II dual MALDI/ESI source and a dynamically harmonized ParaCell (Bruker Daltonics, Billerica, MA). The MALDI source employs a Smartbeam II Nd:YAG laser system (2 kHz, 355 nm). Each protein standard mass spectrum was acquired by manually performing a random raster of a MALDI spot for 8000 laser shots. Data were collected from m/z 1500 to 30 000 with a resolving power ($m/\Delta m$) of ~48 000 at $m/z \sim$ 17 000 unless otherwise noted (using a 6.71 s time-domain transient length) and visualized using Compass DataAnalysis 5.0 (Bruker Daltonics). The most abundant isotopic mass was selected to determine the ion intensities for the protein standard experiments. The ion optics were tuned to maximize high m/z ion transmission, including the funnel RF amplitude (285 V_{pp}), quadrupole (RF-only mode, Q1 mass: m/z 1000), source octopole (2 MHz, 525 V_{pp}), collision cell (collision voltage: −8.0 V; cell: 1.4 MHz, 1900 V_{pp}), time-of-flight delay (3.2 ms), and transfer optics (1 MHz, 410 V_{pp}). The funnel RF amplitude setting is close to the upper software limit of this element. The source DC optics were kept constant for all experiments (capillary exit: 250 V, deflector plate: 200 V, plate offset: 100 V, funnel 1: 150 V, skimmer 1: 70 V). Gated trapping was used in the ICR cell to more efficiently trap high m/z species:[43,45,46] the initial front and rear trapping potentials were set to 2.5 V and ramped down to 1.5 V in 10 ms before ion detection. Ion detection was performed using a sweep excitation power of 50%.

The source region of the instrument is backed by a rough pump and uses atmospheric gas admitted from the open ESI source to maintain a pressure of ~2.9 Torr (~3.9 mbar) in the source region. To regulate the pressure and gas flow in the source region of the instrument, three minor modifications were made to the gas manifold (Figure 1). First, an isolation valve (KF25 aluminum bellows block valve from Agilent Varian, Santa Clara, CA) was inserted between the source rough pump and the vacuum housing. Second, a secondary rough pump (E2M28 rotary vane pump from Edwards, Burgess Hill, England) was added to the source region. The conductance of this secondary pump was also controlled using an isolation valve. A Pirani convection vacuum gauge (CVM211 Stinger from InstruTech, Longmont, CO) was added to accurately

DOI: 10.1021/acs.analchem.7b05105
Anal. Chem. 2018, 90, 5090−5099

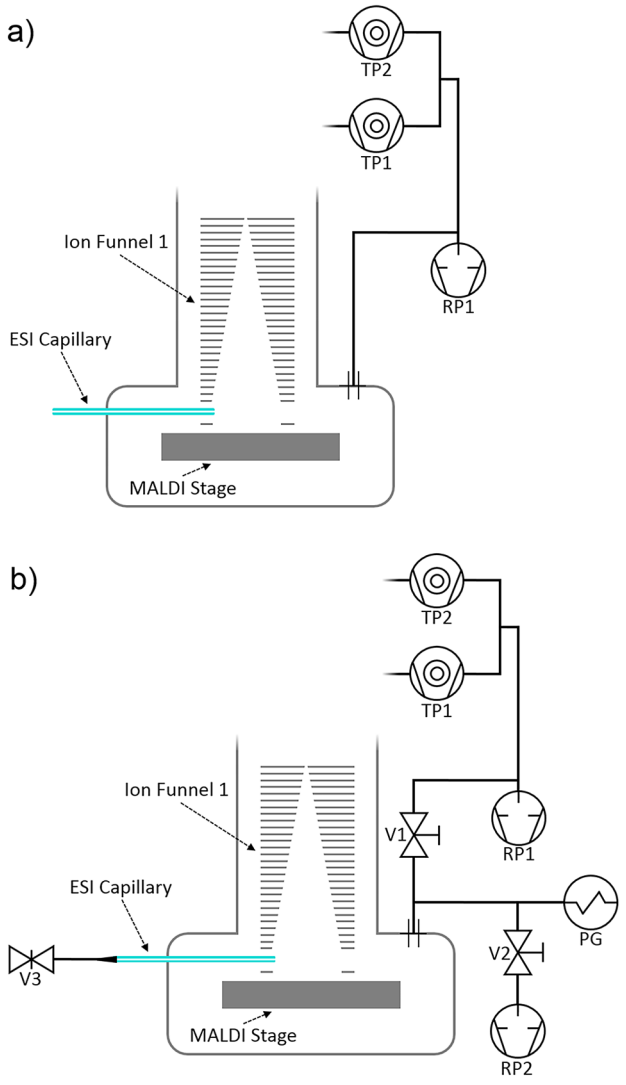

Figure 1. Schematic of selected components in the instrument source region (not to scale) showing (a) the normal gas manifold and (b) the gas manifold that has been modified to incorporate isolation valves (V1 and V2), an additional source rough pump (RP2), a Pirani gauge (PG), and a valve to regulate gas flow through the ESI capillary (V3).

measure the pressure in the source region. However, the measured pressure is likely somewhat different than the actual pressure in the ion funnel, which can vary locally within the device.[19] Finally, the conductance through the ESI capillary was regulated by removing the ESI source and fitting a push-connection of flexible tubing over the end of the ESI capillary. The other end of this tubing was connected to a metering valve (Swagelok, Solon, OH) to regulate the gas flow into the source region. While the connection to the ESI capillary was not a perfect seal, the fitting was sufficient to provide a minimum source pressure of ~250 mTorr (~0.33 mbar) when the metering valve was completely closed. For all experiments herein, altering the source pressure had a minimal effect on the pressure of the downstream collision cell and ICR cell.

Imaging Mass Spectrometry. Transverse sections of rat brain and coronal sections of rat kidney were collected at 12 μm using a Cryostar NX70 Cryostat (Thermo Fisher Scientific, San Jose, CA) and thaw mounted onto indium tin oxide (ITO)-coated slides. Slides containing the tissue sections were washed to remove salts and lipids as previously described.[47] Briefly, the wash protocol consisted of 70% ethanol (30 s), 100% ethanol (30 s), Carnoy's fluid (6:3:1 ethanol:chloroform:acetic acid, 2 min), 100% ethanol (30 s), water (30 s), and 100% ethanol (30 s). Following the wash, samples were dried using a desktop vacuum desiccator for 30 min. A DHA matrix layer was then applied to the slides using a custom-built sublimation apparatus (110 °C, 4.5 min, < 70 mTorr).[48] Immediately prior to IMS analysis, a matrix recrystallization step was performed to improve protein sensitivity (using 1 mL of 1:1, TFA:H_2O for 3 min at 37 °C).[49] Images were acquired at a pixel spacing of 100 μm (for brain tissue) and 60 μm (for kidney tissue) in both the x and y dimensions using a ~75-μm laser beam (1000 laser shots).[50] Data were collected from m/z 1000 to 30 000 using a 4.47 s time-domain transient length. This shorter length transient compared to the protein standard experiments detailed above decreased the time required for image acquisition and resulted in a resolving power of ~41 000 at m/z ~ 17 000. The resulting ion images were visualized using FlexImaging 5.0 (Bruker Daltonics, Billerica, MA), and images are displayed using root-mean-square (RMS) normalization. All ion images were visualized using interpolation except those displayed as part of the image fusion workflow. Following image acquisition, tissue sections were stained using hematoxylin and eosin (H&E) and scanned using a SCN400 brightfield digital whole slide scanner (Leica Microsystems, Bannockburn, IL).

Data-Driven Multimodal Image Fusion. The availability of both IMS and microscopy measurements (albeit with different pixel sizes) enables the use of data-driven image fusion as a means of cross-modal prediction.[51] Briefly, the mass spectra were normalized on the basis of their total ion current, and baseline corrected using a piecewise cubic approximation of the baseline at the 10% quantile of ion intensities, while employing a window size of 100 and a step size of 50. The spectra were subsequently peak-picked to produce an IMS data source of 1156 peak ion images, consisting of 11 129 on-tissue pixels in total and 1704 pixels within the highlighted tissue area. These steps were performed using the Bioinformatics Toolbox of MATLAB (MathWorks). The microscopy data source was an H&E stain of a tissue section serial to the section sampled by IMS and consists natively of the standard red, green, and blue intensity bands, which are subsequently expanded to 905 bands using the transformations described previously.[51] The microscopy source consists of 2 928 451 pixels, 166 848 of which fall within the highlighted area. The IMS and microscopy data sources were spatially registered to each other using a similarity transformation (allows translation, rotation, and scaling), as determined by manual selection of corresponding fiducials in MATLAB using the cpselect() and cp2tform() functions. The mapping step of the fusion process employed an integer 2-D Gaussian bell curve centered on the IMS pixel to map microscopy to IMS measurements.

The fusion process consists of a model building and evaluation phase followed by a prediction phase that then performs the actual estimation of higher-resolution distributions. The modeling phase empirically learns a partial least-squares linear regression model from the linked IMS and microscopy measurements, yielding an IMS/microscopy model that captures how the ion intensity of certain ion species changes when the values of one or more microscopy variables change. The reliability of this model in capturing relationships between observations in IMS and observations in microscopy is

DOI: 10.1021/acs.analchem.7b05105
Anal. Chem. 2018, 90, 5090−5099

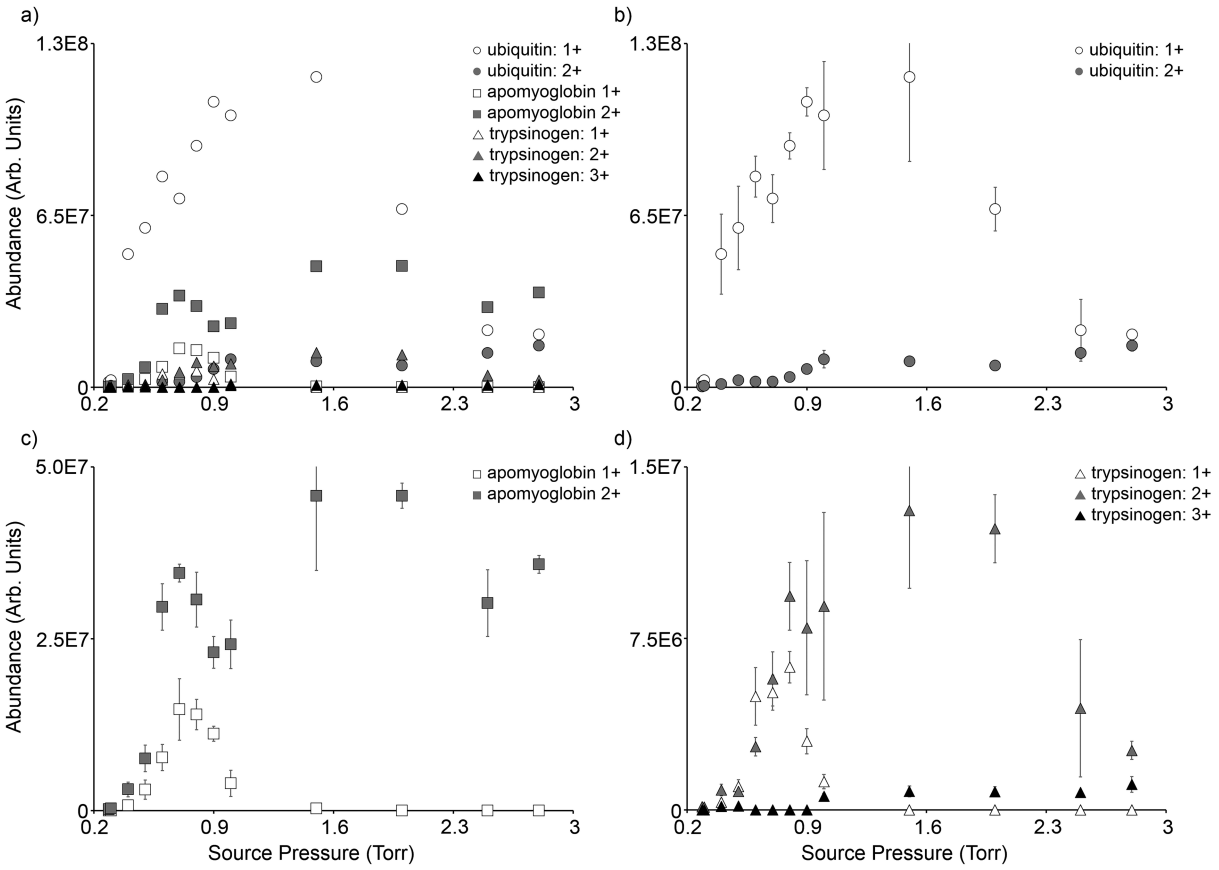

Figure 2. (a) Protein abundance as a function of source pressure for (b) ubiquitin, (c) apomyoglobin, and (d) trypsinogen. In parts b, c, and d, the error bars represent the standard deviation of three replicates. The source pressure was varied by adjusting gas flow through the ESI capillary (V3), and the ESI source is positioned to minimize the overlap with the MALDI ion generation region (Figure S1b).

evaluated for each mass spectral peak individually using several figures of merit (e.g., reconstruction scores).[51] Prediction to a higher spatial resolution is performed only for those ions that are identified to have high predictive capability. For example, in the workflow described here, m/z 7650.009, 13 776.35, and 14 313.60 all yielded good connection to the H&E microscopy, as reported by reconstruction scores of 84.47%, 86.11%, and 79.35%, respectively. For these ions, the prediction phase of the fusion workflow performed prediction to 10-μm spatial resolution.

RESULTS AND DISCUSSION

Systematic Study of Source Pressure. To maximize the transmission efficiency of MALDI-generated protein ions, we sought to optimize both the operating pressure of the ion funnel as well as effects of off-axis gas flow from the ESI capillary. In an effort to minimize the effects of the off-axis gas flow, the ESI source was raised to its maximum adjustable position, reducing the overlap with the MALDI ion generation region (Figure S1). MALDI mass spectra of a mixture of protein standards were then acquired as a function of source pressure, which was controlled by adjusting the valve attached to the ESI capillary (V3). In this configuration, both the V1 and V2 isolation valves are fully open. In general, the abundance of most protein ions increased as the source pressure was decreased from the normal operating pressure of ~2.9 Torr (~3.9 mbar) to ~800 mTorr (~1.1 mbar) (Figure 2). This effect is especially pronounced for the high m/z protein species, namely the singly charged ubiquitin (Figure 2b), apomyoglobin (Figure 2c), and trypsinogen cations (Figure 2d). This increase in ion transmission efficiency at lower pressures is consistent with a greater effective potential wall confining the radial motions of the ions within the funnel.[15,16] Changes in axial gas flow dynamics and the axial DC gradient as they relate to the observed increases in ion transmission efficiency are thought to be minor under these operating conditions.[15,16,19,52] The most efficient ion transmission for the largest m/z species (singly charged apomyoglobin and singly charged trypsinogen) occurs between 700 and 800 mTorr. The abundance of these ions, as well as $[\text{trypsinogen} + 2\text{H}]^{2+}$, is improved by at least 1 order of magnitude compared to that at the normal source operating pressure (Figure 3). The signal-to-noise (S/N) improvement is especially dramatic for singly charged apomyoglobin and singly charged trypsinogen ions not observed at normal source pressure but now readily detected.

The signal intensity of the lower m/z species, namely $[\text{ubiquitin} + 2\text{H}]^{2+}$, $[\text{apomyoglobin} + 2\text{H}]^{2+}$, and $[\text{trypsinogen} + 3\text{H}]^{3+}$, is relatively unchanged as the pressure is decreased from 2.9 to 1.0 Torr. However, the transmission efficiency of the multiply charged ions noticeably decreases as the pressure is reduced further below 1.0 Torr. This difference in transmission between singly and multiply charged species is consistent with the effective potential being higher for multiply charged ions.[15,20] The effective potential in vacuum at point (r, x) in cylindrical coordinates has been defined as

DOI: 10.1021/acs.analchem.7b05105
Anal. Chem. 2018, 90, 5090−5099

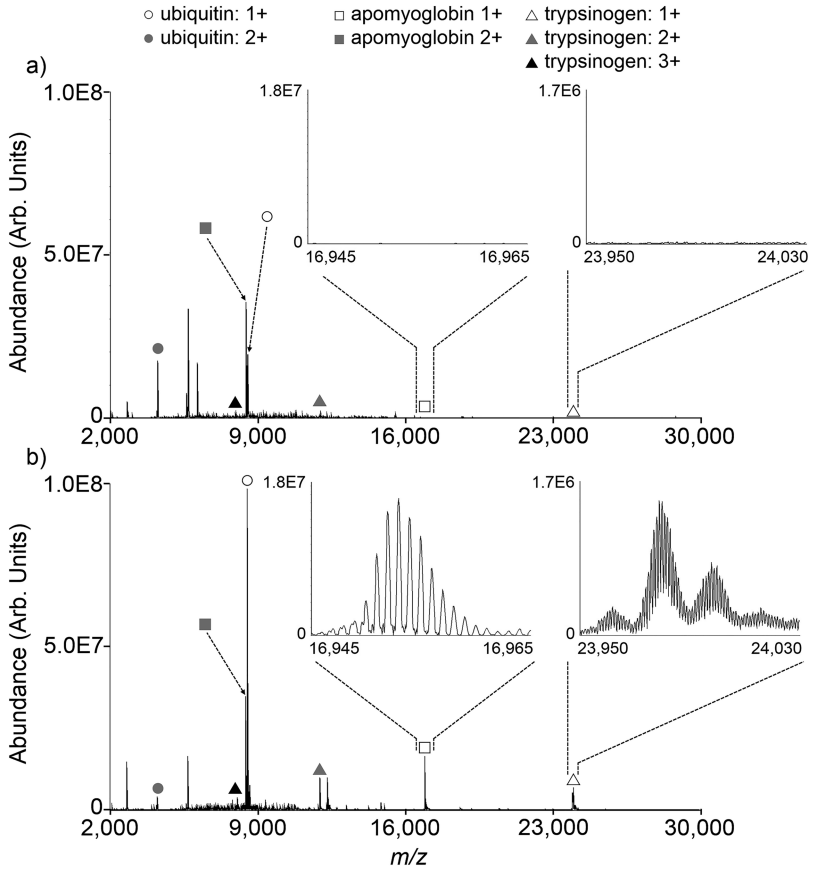

Figure 3. Representative protein standard mass spectra acquired at source pressures of (a) 2.9 Torr and (b) 800 mTorr. The source pressure was varied by adjusting gas flow through the ESI capillary (V3), and the ESI source is positioned to minimize the overlap with the MALDI ion generation region (Figure S1b).

$$V^*(r, x) = \frac{q^2 E_{RF}^2(r, x)}{4m\omega^2} \sim \frac{z^2 V_{RF}^2}{f^2} \quad (1)$$

where $q = ze$ is the charge of the ion, $E_{RF}(r,x)$ is the local RF amplitude and is proportional to the RF voltage applied to the funnel (V_{RF}), m is the mass of the ion, $\omega = 2\pi f$ is the angular frequency, and z is the charge of the ion.[16,20] According to eq 1, the effective potential is proportional to the square of the ion charge state, which supports the charge-state-dependent curves in Figure 2. As the effective potential increases, a low-mass cutoff effect (LMCO), analogous to that observed in RF multipole devices, appears to affect the stability of the lower m/z protein species. While the formation of multiply charged protein ions by MALDI has been shown by several groups to be more favorable at higher pressures,[30,53−57] a pressure-dependent shift in the charge-state distribution of ions produced during the MALDI process seems unlikely here given that there is no concomitant decrease in abundance of the multiply charged species while the higher m/z singly charged species increase in abundance as the pressure is decreased from 2.9 to 1.0 Torr.

When the ESI source is lowered to maximize the overlap with the MALDI ion generation region, the abundance of most protein species again increases as the source pressure is decreased from the normal operating pressure (~2.9 Torr) to ~800 mTorr (Figure S2). However, the increased overlap of the gas flow through the ESI capillary with the MALDI ion generation region appears to disrupt the efficiency of ion collection by the ion funnel. In general, the abundances of the protein species are ~20−40% lower at each pressure in this experiment compared to the those in Figure 2, and a dramatic loss in sensitivity is observed as V3 is opened to pressures above 1.0 Torr.

To examine the effect of pressure on transmission efficiency in the absence of off-axis gas flow, V3 was closed and the pressure was systematically increased by varying V1 (V2 is closed). This minimizes the disruption of ion sampling into the funnel by largely eliminating the gas flow through the ESI capillary. Without further modifications to the vacuum system, the highest achievable pressure using this setup is 800 mTorr. For this experiment, the source was again raised to minimize overlap between the ESI capillary and the MALDI ion generation region. As the source pressure is increased from 300 to 800 mTorr, protein signal is improved (Figure S3), similar to the experiments in which the pressure was manipulated by adjusting V3. The signal abundances between the two sets of experiments are comparable, confirming that there is not a significant disruption of ion focusing induced by the off-axis gas flow in Figure 2. Also evident in Figure S3 is a difference in transmission between singly and multiply charged species. Although there are no data for source pressures above 800 mTorr, this observation is again consistent with the effective potential being higher for multiply charged ions (eq 1). Finally, there is no significant difference in protein signal abundances due to the ESI source position (i.e., ESI capillary not in line with the MALDI generation region (Figure S3) versus ESI capillary in line with the MALDI generation region (Figure S4). This is expected, as there is minimal off-axis gas

DOI: 10.1021/acs.analchem.7b05105
Anal. Chem. 2018, 90, 5090−5099

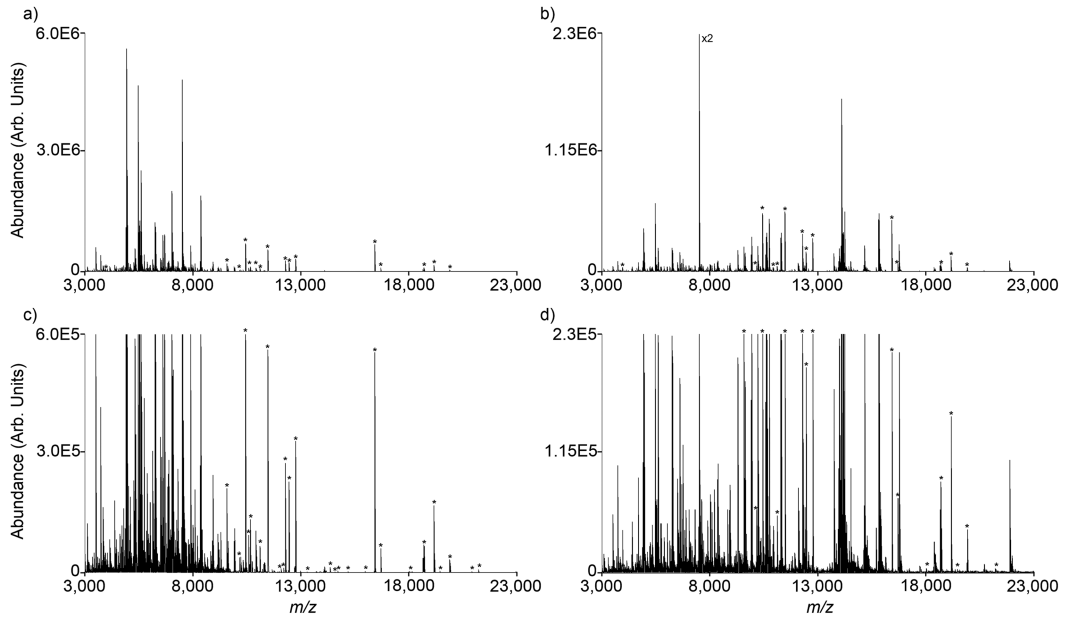

Figure 4. Average mass spectra from rat brain tissue imaging mass spectrometry experiments acquired at source pressures of (a) 2.9 Torr and (b) 750 mTorr. The source pressure was varied by adjusting gas flow through the ESI capillary (V3), and the ESI source was positioned to minimize the overlap with the MALDI ion generation region (Figure S1b). Spectra were background subtracted, and asterisks (*) are used to denote peaks due to electronic noise. (c and d) 10-fold expansions of the intensity scales of parts a and b, respectively.

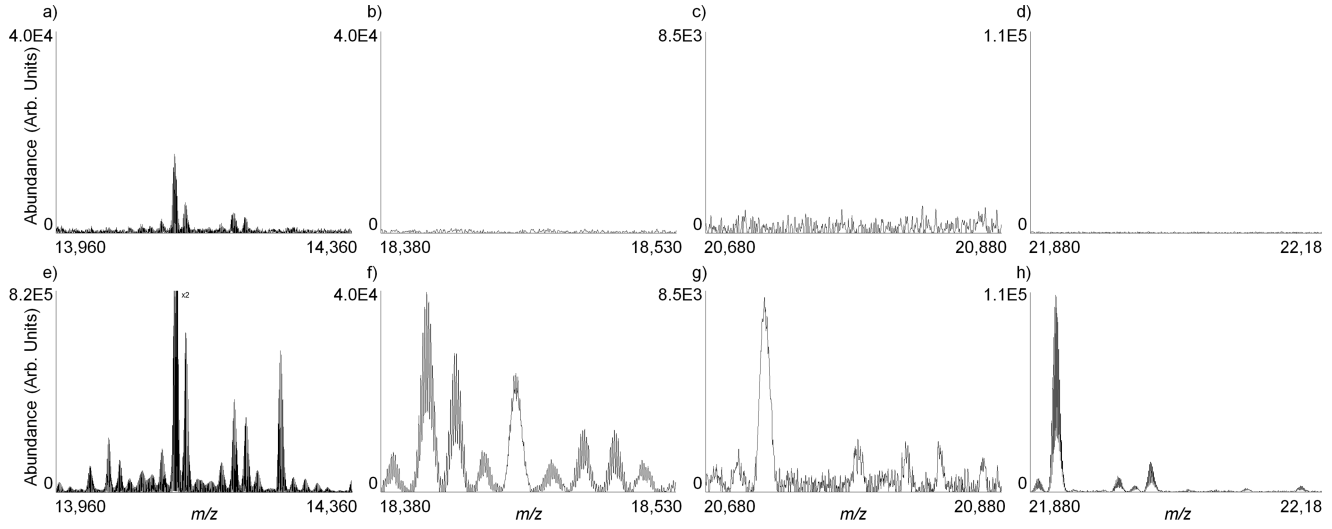

Figure 5. Selected mass ranges from Figure 4 showing average mass spectra from rat brain tissue imaging mass spectrometry acquired at source pressures of (a–d) 2.9 Torr and (e–h) 750 mTorr. The source pressure was varied by adjusting gas flow through the ESI capillary (V3), and the ESI source wass positioned to minimize the overlap with the MALDI ion generation region (Figure S1b).

flow emanating from the ESI source when V3 is closed and the source pressure adjusted using V1. Only when the ESI source is positioned in line with the MALDI ion generation region and V3 opened above roughly 1.0 Torr is the off-axis gas flow sufficient to disrupt ion focusing into the funnel (Figure S2).

Tissue Imaging and Image Fusion. The high mass resolution and accurate mass capabilities of FT-ICR MS have recently been used to facilitate protein identification in imaging mass spectrometry experiments.[32,40,41] While this technology is promising for the identification of post-translational modifications (PTMs) and the separation of overlapping proteoforms, proteins detected with good signal-to-noise ratios in these studies have been limited to m/z values of less than 15 000. Here, we have applied the source conditions optimized as described above for high m/z ion transmission to a protein imaging experiment. One half of a transverse rat brain section was imaged using normal source conditions (2.9 mTorr) while the second half of the brain was imaged under reduced source pressure conditions (750 mTorr). Under normal source conditions, most of the protein species detected are in the mass range of m/z 4000 to 8500, with a few species detected up to $m/z \sim$ 14 000 with low S/N (Figure 4a). However, upon adjusting the source pressure to 750 mTorr using V3, protein signals with good S/N are observed from m/z 4000 to 22 000 (Figure 4b). Dramatic improvements in S/N are observed at high m/z. For example, the abundance of the singly charged species at m/z 14,121.73 is improved by roughly 100-fold using the reduced source pressure (Figure 5a and 5e). Additionally,

DOI: 10.1021/acs.analchem.7b05105
Anal. Chem. 2018, 90, 5090–5099

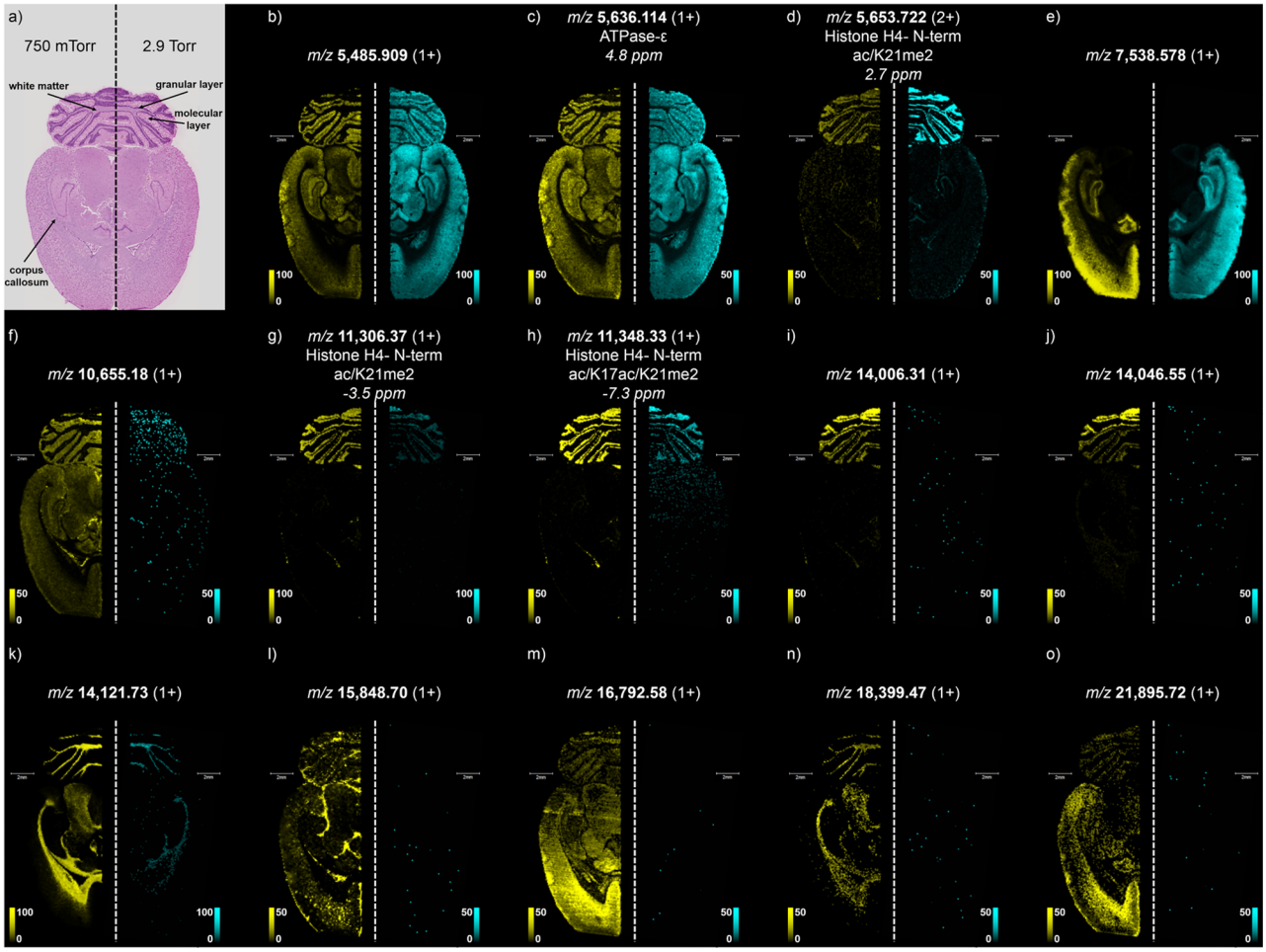

Figure 6. Selected ion images of intact proteins from the mass spectra displayed in Figure 5. (a) An H&E stain of a serial tissue section allows for visualization of brain substructures and indicates the hemispheres of the brain that were analyzed using normal source pressure (right hemisphere) or reduced pressure source conditions (left hemisphere). (b–o) The accurate mass of the most abundant isotope and the protein charge state are reported for each of the ion images. Internal mass calibration was performed using singly and doubly charged species of cytochrome c and hemoglobin α using a quadratic fit. Images are displayed using root-mean-square (RMS) normalization. Ion images are plotted as ±0.25 Da for the most intense isotope. Scale bars = 2 mm.

many other high m/z species that were not detected at normal source pressure are observed with good S/N using a source pressure of 750 mTorr (Figure 5b–d and 5f–h). The isotopic envelopes centered at m/z 18 444.60 and 20 712.00 appear to represent doubly charged species, indicating that the reduced source pressure condition has enabled the detection of proteins with molecular weights over 40 kDa, though the incomplete resolution of these isotopic distributions cannot preclude the presence of two overlapping singly charged proteins (Figure 5f and 5g). Given the results from the protein standard experiments in Figure 2, it is likely that the abundances of protein species below m/z ~ 11 000 are being slightly attenuated at a source pressure of 750 mTorr (attributed to a LMCO effect). Similar to the protein standard experiments, the transmission efficiency for multiply charged species is diminished more so than that for singly charged species at lower m/z, which is consistent with the effective potential in the ion funnel being higher for multiply charged species (Figure S5). A more optimal source pressure for ions in this mass range is ~1.0 Torr. However, in this imaging experiment we sought to maximize the transmission of the highest m/z species, which occurs at a source pressure of ~750 mTorr.

Despite the signal attenuation observed for ions at lower m/z, ion images can be produced across a broad mass range from m/z 4000 to 22 000 using the reduced source pressure, roughly doubling the mass range for which quality protein ion images can be produced (Figure 6). While the image quality for proteins in the lower m/z range is comparable between the two source conditions (Figure 6b–e), the image quality for proteins above m/z ~ 9000 is dramatically improved at reduced source pressure (Figure 6f–o). The spatial distributions of proteins up to m/z ~ 22 000 are clearly visible in many brain substructures including the corpus callosum, white matter, granular layer, and molecular layer. The high mass resolving power of the FT-ICR platform allows for clear isotopic resolution of most of these high m/z protein species, and ion images are plotted using a ±0.25 Da window of the most intense isotope to minimize interferences from potentially overlapping isotopic patterns. Using accurate mass measurements, tentative identifications for selected ions can be made based on previous reports of rat brain protein imaging. For example, the protein ion detected at m/z 5,636.114 can be tentatively identified as ATP synthase subunit epsilon (Figure 6c, 4.8 ppm).[32] Similarly, the protein at m/z 11 348.33 can be tentatively identified as doubly acetylated and dimethylated histone H4 (Figure 6h, −7.3 ppm). These

DOI: 10.1021/acs.analchem.7b05105
Anal. Chem. 2018, 90, 5090–5099

post-translational modifications have previously been identified by top-down proteomics (N-terminal acetylation, acetylation of lysine 17, and dimethylation of lysine 21).[32] Finally, the ions at m/z 5653.722 and m/z 11 306.37 are tentatively identified as doubly (2.7 ppm) and singly charged (−3.5 ppm) versions of histone H4 that has an N-terminal acetylation and dimethylation of lysine 21 (Figure 6d and 6g).[32] Imaging mass spectrometry analysis of rat kidney tissue was also performed at a reduced source pressure, enabling the detection of protein ions up to $m/z \sim 17\,000$ (Figure S6). Similar to IMS analysis of rat brain tissue, high quality ion images are obtained here for species above $m/z \sim 9000$ (Figure S7). Doubly charged ions are observed up to m/z 11,654.37, allowing for the mapping of protein species of molecular weights in excess of 23 kDa (Figure S7d).

While the FT-ICR platform facilitates the identification of proteins in an imaging experiment, the length of the time-domain signal required to adequately resolve these high m/z ions is significant. The 4.47 s transient length used in the imaging experiment shown in Figure 6 provided for a resolving power of ∼41 000 at $m/z \sim 17\,000$ but necessitated over 28 h of instrument time to complete the two 100 μm protein imaging experiments. As the number of pixels, and thus image acquisition time, required to sample a given area of tissue is inversely proportional to the square of the pixel size,[58−62] protein imaging mass spectrometry at higher spatial resolutions using FT-ICR MS quickly becomes time-prohibitive. There is thus specific interest in using data-driven FT-ICR IMS-microscopy image fusion[51] to predict protein ion distributions to a higher spatial resolution than that of the original IMS experiment. To assess the feasibility of this approach, we performed a "spatial sharpening" application of data-driven image fusion, which predicts protein ion distributions to a spatial resolution that exceeds that of the measured ion images by 10-fold. In this workflow, the IMS protein measurements acquired at 100-μm spatial resolution are fused with the H&E microscopy measurements acquired at 10-μm spatial resolution to predict protein ion distributions at 10-μm spatial resolution (Figure 7). This results in a single predictive image modality with FT-ICR-grade molecular specificity and microscopy-grade spatial resolution. These predicted images are accompanied by "reconstruction scores," which are numerical measures of confidence that help assess the reliability of each of the ion distribution estimations.[51] For example, the successful predictions of protein ions at m/z 7,650.009, 13,776.35, and 14 313.60 to 10 μm is confirmed with relatively high reconstruction scores of 84.47%, 86.11%, and 79.35%, respectively (Figure 7c and Figures S8−10). This proof-of-concept application demonstrates the compatibility of high m/z protein FT-ICR IMS with in silico up-sampling techniques such as data-driven image fusion, which outperforms common bilinear interpolation (Figures S8−10). This example illustrates that predictive computational methods hold potential to offset some of the practical constraints incurred by the longer time-domain transient lengths and limited spatial resolutions used in this work.

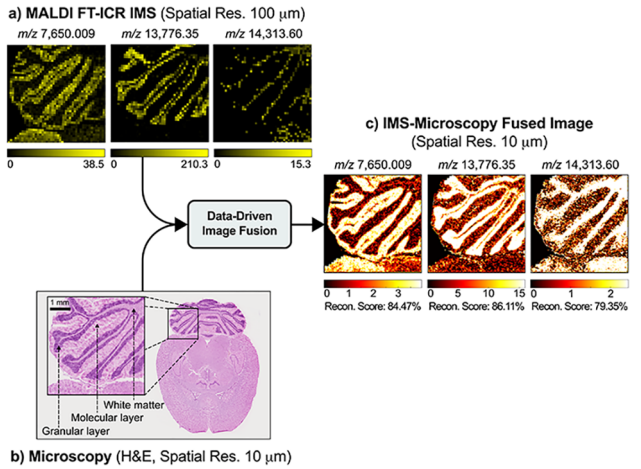

Figure 7. Data-driven, multimodal image fusion of (a) FT-ICR IMS data acquired at 100-μm spatial resolution with (b) H&E microscopy measurements acquired at 10-μm spatial resolution to predict (c) protein ion distributions at 10-μm spatial resolution. Three protein species with relatively good reconstruction scores (>75%) are exemplified here.

CONCLUSIONS

Modifications to the gas manifold of a 15T FT-ICR MS have enabled control of the gas flow and pressure in the MALDI source region. A systematic evaluation of the effect of source pressure on ion transmission efficiency through the ion funnel found that reducing the source pressure from 2.9 Torr to 750 mTorr improved the transmission efficiency of high m/z protein species by 10- to 100-fold. This improvement is attributed to a less dampened effective potential for ion radial confinement at reduced pressures and has enabled the detection of protein standard ions up to m/z 24 000. Other observations consistent with previous ion funnel reports, including a LMCO effect and differences in the transmission efficiencies of singly and multiply charged ions, are also noted. The newly optimized source conditions have been used in an imaging experiment to roughly double the mass range for which high quality protein ion images can be acquired from rat brain and kidney tissue. The high resolution accurate mass capabilities of FT-ICR MS have facilitated the identification of proteins detected in the imaging data. We have used a computational tool, FT-ICR IMS-microscopy image fusion, to mitigate the long acquisition time associated with FT-ICR protein imaging and produce protein images that have both high mass resolution and high spatial resolution.

ASSOCIATED CONTENT

Supporting Information

The Supporting Information is available free of charge on the ACS Publications website at DOI: 10.1021/acs.analchem.7b05105.

Additional Figures S1−10 (PDF)

AUTHOR INFORMATION

Corresponding Author

*Phone: (615) 343-7333. Fax: (615) 343-8372. E-mail: jeff.spraggins@vanderbilt.edu.

ORCID

Boone M. Prentice: 0000-0002-1927-9457
Daniel J. Ryan: 0000-0001-8201-1472
Raf Van de Plas: 0000-0002-2232-7130
Richard M. Caprioli: 0000-0001-5859-3310
Jeffrey M. Spraggins: 0000-0001-9198-5498

DOI: 10.1021/acs.analchem.7b05105
Anal. Chem. 2018, 90, 5090−5099

Notes

The authors declare no competing financial interest.

■ ACKNOWLEDGMENTS

This work was supported by the National Institutes of Health (NIH) under awards P41 GM103391-07 (National Institute of General Medical Sciences [NIGMS]) and 1S10OD012359-01 (National Institutes of Health Shared Instrumentation Grant Program). The authors also thank Dr. Jeremy Wolff of Bruker Daltonics for input regarding the source gas manifold modifications.

■ REFERENCES

(1) Dole, M.; Mack, L. L.; Hines, R. L.; Mobley, R. C.; Ferguson, L. D.; Alice, M. B. *J. Chem. Phys.* **1968**, *49*, 2240−2249.
(2) Mack, L. L.; Kralik, P.; Rheude, A.; Dole, M. *J. Chem. Phys.* **1970**, *52*, 4977−4986.
(3) Yamashita, M.; Fenn, J. B. *J. Phys. Chem.* **1984**, *88*, 4451−4459.
(4) Fenn, J. B.; Mann, M.; Meng, C. K.; Wong, S. F.; Whitehouse, C. M. *Science* **1989**, *246*, 64−71.
(5) Bruins, A. P.; Covey, T. R.; Henion, J. D. *Anal. Chem.* **1987**, *59*, 2642−2646.
(6) Chowdhury, S. K.; Katta, V.; Chait, B. T. *Rapid Commun. Mass Spectrom.* **1990**, *4*, 81−87.
(7) Wilm, M. S.; Mann, M. *Int. J. Mass Spectrom. Ion Processes* **1994**, *136*, 167−180.
(8) Wilm, M.; Mann, M. *Anal. Chem.* **1996**, *68*, 1−8.
(9) Shaffer, S. A.; Tang, K.; Anderson, G. A.; Prior, D. C.; Udseth, H. R.; Smith, R. D. *Rapid Commun. Mass Spectrom.* **1997**, *11*, 1813−1817.
(10) Shaffer, S. A.; Prior, D. C.; Anderson, G. A.; Udseth, H. R.; Smith, R. D. *Anal. Chem.* **1998**, *70*, 4111−4119.
(11) Kim, T.; Tolmachev, A. V.; Harkewicz, R.; Prior, D. C.; Anderson, G.; Udseth, H. R.; Smith, R. D.; Bailey, T. H.; Rakov, S.; Futrell, J. H. *Anal. Chem.* **2000**, *72*, 2247−2255.
(12) Second, T. P.; Blethrow, J. D.; Schwartz, J. C.; Merrihew, G. E.; MacCoss, M. J.; Swaney, D. L.; Russell, J. D.; Coon, J. J.; Zabrouskov, V. *Anal. Chem.* **2009**, *81*, 7757−7765.
(13) Fernandez-Lima, F.; Kaplan, D. A.; Suetering, J.; Park, M. A. *Int. J. Ion Mobility Spectrom.* **2011**, *14*, 93−98.
(14) May, J. C.; Goodwin, C. R.; Lareau, N. M.; Leaptrot, K. L.; Morris, C. B.; Kurulugama, R. T.; Mordehai, A.; Klein, C.; Barry, W.; Darland, E.; Overney, G.; Imatani, K.; Stafford, G. C.; Fjeldsted, J. C.; McLean, J. A. *Anal. Chem.* **2014**, *86*, 2107−2116.
(15) Lynn, E. C.; Chung, M. C.; Han, C. C. *Rapid Commun. Mass Spectrom.* **2000**, *14*, 2129−2134.
(16) Tolmachev, A. V.; Kim, T.; Udseth, H. R.; Smith, R. D.; Bailey, T. H.; Futrell, J. H. *Int. J. Mass Spectrom.* **2000**, *203*, 31−47.
(17) Julian, R. R.; Mabbett, S. R.; Jarrold, M. F. *J. Am. Soc. Mass Spectrom.* **2005**, *16*, 1708−1712.
(18) Page, J. S.; Tolmachev, A. V.; Tang, K. Q.; Smith, R. D. *J. Am. Soc. Mass Spectrom.* **2006**, *17*, 586−592.
(19) Kelly, R. T.; Tolmachev, A. V.; Page, J. S.; Tang, K. Q.; Smith, R. D. *Mass Spectrom. Rev.* **2010**, *29*, 294−312.
(20) Ibrahim, Y.; Tang, K. Q.; Tolmachev, A. V.; Shvartsburg, A. A.; Smith, R. D. *J. Am. Soc. Mass Spectrom.* **2006**, *17*, 1299−1305.
(21) Dehmelt, H. G. In *Advances in Atomic and Molecular Physics*; Bates, D. R.; Estermann, I., Eds.; Academic Press: New York, 1967; pp 53−72.
(22) Gerlich, D. In *State-Selected and State-to-State Ion−Molecule Reaction Dynamics. Part 1: Experiment*; Ng, C.-Y.; Baer, M., Eds.; John Wiley & Sons, Inc.: New York, 1992.
(23) Schmidt, A.; Bahr, U.; Karas, M. *Anal. Chem.* **2001**, *73*, 6040−6046.
(24) van den Heuvel, R. H. H.; van Duijn, E.; Mazon, H.; Synowsky, S. A.; Lorenzen, K.; Versluis, C.; Brouns, S. J. J.; Langridge, D.; van der Oost, J.; Hoyes, J.; Heck, A. J. R. *Anal. Chem.* **2006**, *78*, 7473−7483.
(25) Landreh, M.; Liko, I.; Uzdavinys, P.; Coincon, M.; Hopper, J. T. S.; Drew, D.; Robinson, C. V. *Chem. Commun.* **2015**, *51*, 15582−15584.
(26) Rosati, S.; Rose, R. J.; Thompson, N. J.; van Duijn, E.; Damoc, E.; Denisov, E.; Makarov, A.; Heck, A. J. R. *Angew. Chem., Int. Ed.* **2012**, *51*, 12992−12996.
(27) van de Waterbeemd, M. V.; Fort, K. L.; Boll, D.; Reinhardt-Szyba, M.; Routh, A.; Makarov, A.; Heck, A. J. R. *Nat. Methods* **2017**, *14*, 283−286.
(28) Li, H. L.; Nguyen, H. H.; Loo, R. R. O.; Campuzano, I. D. G.; Loo, J. A. *Nat. Chem.* **2018**, *10*, 139−148.
(29) Karas, M.; Kruger, R. *Chem. Rev.* **2003**, *103*, 427−439.
(30) Knochenmuss, R.; Zenobi, R. *Chem. Rev.* **2003**, *103*, 441−452.
(31) Knochenmuss, R. *Analyst* **2006**, *131*, 966−986.
(32) Spraggins, J. M.; David, R. G.; Jessica Moore, L.; Kristie Rose, L.; Neal Hammer, D.; Eric Skaar, P.; Richard Caprioli, M. *J. Am. Soc. Mass Spectrom.* **2015**, *26*, 974−985.
(33) Baykut, G.; Jertz, R.; Witt, M. *Rapid Commun. Mass Spectrom.* **2000**, *14*, 1238−1247.
(34) Belov, M. E.; Gorshkov, M. V.; Udseth, H. R.; Anderson, G. A.; Tolmachev, A. V.; Prior, D. C.; Harkewicz, R.; Smith, R. D. *J. Am. Soc. Mass Spectrom.* **2000**, *11*, 19−23.
(35) Kellersberger, K. A.; Tan, P. V.; Laiko, V. V.; Doroshenko, V. M.; Fabris, D. *Anal. Chem.* **2004**, *76*, 3930−3934.
(36) Tan, P. V.; Laiko, V. V.; Doroshenko, V. M. *Anal. Chem.* **2004**, *76*, 2462−2469.
(37) Smith, D. F.; Aizikov, K.; Duursma, M. C.; Giskes, F.; Spaanderman, D. J.; McDonnell, L. A.; O'Connor, P. B.; Heeren, R. M. A. *J. Am. Soc. Mass Spectrom.* **2011**, *22*, 130−137.
(38) Karas, M.; Hillenkamp, F. *Anal. Chem.* **1988**, *60*, 2299−2301.
(39) Tanaka, K.; Waki, N.; Ido, Y.; Akita, S.; Yoshida, Y.; Yoshida, T.; Matsuo, T. *Rapid Commun. Mass Spectrom.* **1988**, *2*, 151−153.
(40) Spraggins, J.; Rizzo, D.; Moore, J.; Noto, M.; Skaar, E.; Caprioli, R. *Proteomics* **2016**, *16*, 1678−1689.
(41) Dilillo, M.; Ait-Belkacem, R.; Esteve, C.; Pellegrini, D.; Nicolardi, S.; Costa, M.; Vannini, E.; de Graaf, E. L.; Caleo, M.; McDonnell, L. A. *Sci. Rep.* **2017**, *7*.10.1038/s41598-017-00703-w
(42) Castro, J. A.; Koster, C.; Wilkins, C. *Rapid Commun. Mass Spectrom.* **1992**, *6*, 239−241.
(43) Koster, C.; Castoro, J. A.; Wilkins, C. L. *J. Am. Chem. Soc.* **1992**, *114*, 7572−7574.
(44) Easterling, M. L.; Mize, T. H.; Amster, I. J. *Anal. Chem.* **1999**, *71*, 624−632.
(45) Alford, J. M.; Williams, P. E.; Trevor, D. J.; Smalley, R. E. *Int. J. Mass Spectrom. Ion Processes* **1986**, *72*, 33−51.
(46) Kofel, P.; Allemann, M.; Kellerhals, H.; Wanczek, K. P. *Int. J. Mass Spectrom. Ion Processes* **1986**, *72*, 53−61.
(47) Deutskens, F.; Yang, J.; Caprioli, R. M. *J. Mass Spectrom.* **2011**, *46*, 568−571.
(48) Hankin, J. A.; Barkley, R. M.; Murphy, R. C. *J. Am. Soc. Mass Spectrom.* **2007**, *18*, 1646−1652.
(49) Yang, J.; Caprioli, R. M. *Anal. Chem.* **2011**, *83*, 5728−5734.
(50) Caprioli, R. M.; Farmer, T. B.; Gile, J. *Anal. Chem.* **1997**, *69*, 4751−4760.
(51) Van de Plas, R.; Yang, J.; Spraggins, J.; Caprioli, R. M. *Nat. Methods* **2015**, *12*, 366−372.
(52) Kim, T.; Udseth, H. R.; Smith, R. D. *Anal. Chem.* **2000**, *72*, 5014−5019.
(53) Zenobi, R.; Knochenmuss, R. *Mass Spectrom. Rev.* **1998**, *17*, 337−366.
(54) Konig, S.; Kollas, O.; Dreisewerd, K. *Anal. Chem.* **2007**, *79*, 5484−5488.
(55) Sampson, J. S.; Hawkridge, A. M.; Muddiman, D. C. *Anal. Chem.* **2008**, *80*, 6773−6778.
(56) Sampson, J. S.; Muddiman, D. C. *Rapid Commun. Mass Spectrom.* **2009**, *23*, 1989−1992.
(57) McEwen, C. N.; Larsen, B. S.; Trimpin, S. *Anal. Chem.* **2010**, *82*, 4998−5001.

DOI: 10.1021/acs.analchem.7b05105
Anal. Chem. 2018, 90, 5090−5099

(58) Spengler, B.; Hubert, M. *J. Am. Soc. Mass Spectrom.* **2002**, *13*, 735−748.
(59) Hopfgartner, G.; Varesio, E.; Stoeckli, M. *Rapid Commun. Mass Spectrom.* **2009**, *23*, 733−736.
(60) Spraggins, J. M.; Caprioli, R. M. *J. Am. Soc. Mass Spectrom.* **2011**, *22*, 1022−1031.
(61) Trim, P.; Djidja, M.-C.; Atkinson, S.; Oakes, K.; Cole, L.; Anderson, D.; Hart, P.; Francese, S.; Clench, M. *Anal. Bioanal. Chem.* **2010**, *397*, 3409−3419.
(62) Prentice, B. M.; Chumbley, C. W.; Caprioli, R. M. *J. Mass Spectrom.* **2015**, *50*, 703−710.

DOI: 10.1021/acs.analchem.7b05105
Anal. Chem. 2018, 90, 5090−5099